Chirped imaging pulses in four-dimensional electron microscopy: femtosecond pulsed hole burning

2012 New J. Phys. 14 053046

(http://iopscience.iop.org/1367-2630/14/5/053046)

New Journal of Physics
The open-access journal for physics

Chirped imaging pulses in four-dimensional electron microscopy: femtosecond pulsed hole burning

Sang Tae Park, Oh-Hoon Kwon and Ahmed H Zewail[1]
Physical Biology Center for Ultrafast Science and Technology, Arthur Amos Noyes Laboratory of Chemical Physics, California Institute of Technology, Pasadena, CA 91125, USA
E-mail: zewail@caltech.edu

New Journal of Physics **14** (2012) 053046 (22pp)
Received 29 March 2012
Published 31 May 2012
Online at http://www.njp.org/
doi:10.1088/1367-2630/14/5/053046

Abstract. The energy and time correlation, i.e. the chirp, of imaging electron pulses in dispersive propagation is measured by time-slicing (temporal hole burning) using photon-induced near-field electron microscopy. The chirp coefficient and the degree of correlation are obtained in addition to the duration of the electron pulse and its energy spread. Improving temporal and energy resolutions by time-slicing and energy-selection is discussed here and we explore their utility in imaging with time and energy resolutions below those of the generated ultrashort electron pulse. Potential applications for these imaging capabilities are discussed.

S Online supplementary data available from stacks.iop.org/NJP/14/053046/mmedia

[1] Author to whom any correspondence should be addressed.

Contents

1. Introduction

The advent of four-dimensional (4D) electron microscopy has made possible the direct study of structural dynamics with atomic-scale spatiotemporal resolutions [1, 2]. The scope of applications is diverse, including the study of chemical bonding dynamics [3], macromolecular conformation changes [4] and nanomechanical vibrations [5]; for a review see [6] and references therein. In these studies, ultrashort electron pulses are utilized in imaging, diffraction and spectroscopy, and it is essential to optimize the spatial and temporal coherence in order to achieve atomic-scale resolutions. In general, the electron pulse may have time-energy phase space correlations which, if realized, could be exploited in controlling the time resolution and energy selectivity in imaging, as shown here.

In conventional microscopes, electrons are generated either by heating a source or by field emission; the beam is a continuous wave made of randomly distributed electrons. With a continuous beam, the structures probed are time-averaged over milliseconds or longer acquisition times and the electrons used are temporally incoherent in these recordings. For the electron pulse, three coherence lengths, determined by the longitudinal and transverse momentum spread (δp_i), are simply given by the following relationship:

$$l_{c,i} = \frac{1}{\delta k_i} = \frac{\hbar}{\delta p_i} \approx \frac{\lambda}{2\pi\ (\delta p_i / p_z)}, \quad \text{for } i = x, y, z; \tag{1}$$

where the total coherence length is given by: $\frac{1}{l_c^2} = \frac{1}{l_{c,z}^2} + \frac{1}{l_{c,x}^2} + \frac{1}{l_{c,y}^2}$. It follows that a typical $\sim$1 eV energy spread at a kinetic energy of 200 keV gives rise to a small longitudinal momentum spread (δp_z), and the electron coherence becomes dominantly determined by the transverse value [7]. However, this transverse coherence for a heated source is relatively poor, and for high resolution, lenses and apertures are introduced in order to reduce the transverse momentum spread and achieve the desired coherence at the specimen (Van Cittert–Zernike concept [8–10]). This leads to a loss in the number of electrons, typically with a throughput of 10^{-1} to 10^{-4} from the source to the specimen.

In 4D electron microscopy, coherence is determined by the properties of the electron pulse that is generated by the femtosecond (fs) optical pulse via the photoelectric (or field-assisted photoelectric) effect. Unlike the randomly distributed electrons in conventional microscopes, the pulses are timed with fs accuracy. Unless each pulse contains a single electron, the space-charge effect [11] will lead to an energy (and time) spread [6]. In this space-charge regime, transverse coherence may still be manipulated using apertures and condenser lenses, because transverse Coulomb repulsion is negligible at the center of the beam (when considering the integration of interactions over the beam cross section) and its magnitude increases as the distance from the center increases. Thus, only a small portion at the center of the beam can be selected for imaging/diffraction with relatively high coherence.

On the other hand, longitudinal Coulomb repulsion induces a momentum spread which cannot be reduced by lenses, and may become the dominant factor in determining the coherence time and length; for energy spreads larger than $\sim$10 eV in a typical microscope, the longitudinal coherence becomes poorer than the transverse counterpart. To maintain the high spatial resolution in the pulsed mode, the number of electrons per pulse is reduced in what is termed as the single-electron regime [6]. In practice, an electron pulse with up to $\sim 10^2$ electrons at the source does not suffer significantly from the space-charge effect (temporal spread), whereas the energy spread begins to increase at $\sim 10^1$ electrons per pulse. The Coulomb repulsion energy, together with the excess energy above the work function, constitutes the total electron-energy spread; for thermionic, Schottky-field emission, and cold-field emission sources the spreads are typically 1.0, 0.6, and 0.3 eV, respectively [12–14]. A monochromator can reduce the energy spread down to 0.15 eV [15], and for pulsed photoelectrons an energy spread of 0.1 eV has been achieved [16].

The energy spread in the pulse can develop a chirp, an energy–time correlation, because the electrons with higher energies lead and those with lower energies lag, depending on the electron distribution at the source (see below); an energy spread of 1 eV can result in a temporal spread of several hundred fs. The uncertainty in position-momentum is related to such broadening, depending on electron speed (v): $\Delta x \Delta p = (\Delta x/v) \cdot (v \Delta p) = \Delta t \Delta E$.

To circumvent pulse broadening, and to compress ultrashort electron pulses, several schemes have been discussed, including the lowering of the excess energy above the work function [17]; energy filtering at the detector, which limits the energy distribution [17, 18]; and the use of a 'reflectron' (an electrostatic mirror), which can reverse the chirp and compress the pulses [7, 19, 20]. Alternatively, radiofrequency (RF) electric fields, a time-dependent acceleration/deceleration, can boost up lagging electrons at the tail of the pulse and retard the leading electrons at the front, leading to a compression of the initial pulse [21, 22]. Using the ponderomotive force of optical pulses, it is possible to design a 'temporal lens' (position-dependent acceleration/deceleration) that can push the trailing electrons and pull the leading electrons, and cause an inverse chirp [23, 24]. The aforementioned methods can also be used to reverse space-charge temporal broadening in multi-electron pulses, and it is even possible to shorten their duration beyond the initial width [18, 25][2]. It follows that understanding

[2] It is to be noted that in order to compress electron pulses shorter than the initial duration, the energy spread has to be increased, because a temporal lens also conserves longitudinal emittance, $\varepsilon_z = \sigma z \delta p_z \approx \sigma t \delta E$, similar to a spatial lens which does not change transverse emittance. Therefore, a compressed pulse may be highly bright yet poorly coherent due to longitudinal coherence. Brightness is defined with transverse emittance only, because for a continuous beam, longitudinal emittance is not applicable due to its continuous nature, and because the

energy–time correlations in electron propagation is essential for maintaining and improving the spatial, temporal and energy resolutions in imaging.

In this paper, we report direct experimental mapping of phase space (energy–time correlations) using photon-induced near-field electron microscopy (PINEM) [26–28] with fs time resolution. Here it is shown that a 'hole' can be burned in the energy distribution of the electron pulse. By invoking a nanostructure (silver wire), the optical pulse creates a near field which enables the coupling between the evanescent photons and electrons. It was possible to establish the chirp relationship between time and energy by following the time-dependent shift of the zero-loss peak (ZLP) and PINEM peaks in the energy spectrum. Temporally shorter and energetically narrower coherent electron pulses, from linearly chirped electron pulses, are obtained by exploiting features of the chirp in the electron microscope. The theoretical analysis supports the experimental findings, and here we only highlight the relevant theoretical concepts of PINEM [28] and of pulse slicing [29].

2. Experimental

The experiments were performed on a collection of silver nanowires with a diameter ranging from 50 to 100 nm. The time-resolved electron energy spectra were recorded using Caltech's second generation ultrafast electron microscope (UEM-2) [30]. The electron source is equipped with a field-emission gun geometry (Tecnai 20, FEI). The tip is replaced by a 16 μm LaB_6 flat cathode, whose work function is $\sim$2.6 eV. A train of 280 fs infrared laser pulses ($\lambda = 1038$ nm) at a repetition rate of 2 MHz was split into two parts, one of which was frequency doubled to give the 519 nm laser pulses that were used to excite the nanostructures at a fluence of 0.5 mJ cm^{-2}. The other beam was frequency quadrupled to produce UV pulses (259 nm, 4.78 eV), which were directed to the photocathode to generate the electron pulses.

The energy spread of the electron pulse can be manipulated by changing the number of electrons and the excess energy above the work function; here we varied the spread from 1.2 eV to 3.5 eV using the former not the latter. The electron pulses were accelerated to 200 keV in the column and dispersed after transmission through the specimen in order to provide the energy spectra of the electrons which interacted with the photons; a 1 mm entrance aperture was used to retain optimal energy resolution. The timing between the optical pump/gate pulse and the electron probe pulse at the specimen was controlled by an optical delay line, as described elsewhere [31].

3. Theoretical: photon-induced near-field electron microscopy of the chirped pulses

In general, electron energy distributions are incoherent due to the emission process in the microscope. This gives rise to velocity distributions that lead to different arrival times at the specimen for electrons with different energy. Accordingly, in the pulsed mode each single-energy packet will experience different temporal overlap with the optical pulse used to excite the nanostructure. The theory for this electron–photon interaction (PINEM description) has been reported for a coherent single-energy packet [28, 29]. In this paper, we formulate the theory for

longitudinal momentum spread is much smaller than the transverse counterpart in conventional TEM, whereas the longitudinal coherence is a function of the longitudinal momentum spread, and hence the energy spread ($\delta E = \sum v_i \delta p_i \approx v_z \delta p_z$).

chirped pulses that have energy distributions. The solution is obtained by solving the time-dependent Schrödinger equation of the electron wavefunction in the space domain and as a function of time. It is, however, more convenient to represent it as the temporal solution of a probability density in the time domain in order to describe the electron dispersion and the temporal coincidence with the optical pulse.

We designate $G(x)$ to be a normalized Gaussian profile along the coordinate, x, with $\bar{x}$ and σ_x being the mean value and standard deviation width, respectively:

$$G(x) = G(x;\bar{x},\sigma_x) = G(x-\bar{x};\sigma_x) = \frac{1}{\sqrt{2\pi}\sigma_x}\exp\left[-\frac{(x-\bar{x})^2}{2\sigma_x^2}\right]. \tag{2}$$

The probability density of a propagating electron packet at a single energy (ignoring coherent dispersion) becomes:

$$P_{\mathrm{e}}(z,t) = G\left(z-v_{\mathrm{e}}t;\, v_{\mathrm{e}}\sigma t_{\mathrm{e}}\right), \tag{3}$$

where v_{e} and σt_{e} are the velocity and the temporal width, respectively. Equation (3) describes the spatial density at a given time, t, or the temporal profile at a given position, z, such that they can be related by $P_{\mathrm{e},t=T}(z)\,|\mathrm{d}z| = P_{\mathrm{e},z=Z}(t)\,|\mathrm{d}t|$ when $z - v_{\mathrm{e}}T = Z - v_e t$; it follows that $t-T = -(z-Z)/v_{\mathrm{e}}$, where T is the time at which the spatial distribution is probed and Z is the position where the temporal profile is considered. Similarly, we assume that the optical intensity at $z = Z$ is given by $I_{\mathrm{p}}(t) \propto I_0 G\left(t-\bar{t}_{\mathrm{p}};\sigma t_{\mathrm{p}}\right)$. Accordingly, at $z = Z$, $\bar{t}_{\mathrm{e}} = \langle t\rangle_{\mathrm{e}} = \int \mathrm{d}t\; t\; P_{\mathrm{e}}(t)$ and $\bar{t}_{\mathrm{p}} = \langle t\rangle_{\mathrm{p}} = \int \mathrm{d}t\; t\; P_{\mathrm{p}}(t)$ become the mean arrival times of an electron packet (moving at v_e) and an optical pulse (moving at c), respectively; $\tau \equiv \bar{t}_{\mathrm{e}} - \bar{t}_{\mathrm{p}}$ is then the delay time between the electron and optical pulses. For convenience, we define $z' \equiv z - v_e t$ as the moving frame coordinate system. Similarly, we define $t' \equiv -z'/v_{\mathrm{e}}$ which corresponds to an 'instantaneous' time that describes the temporal profile of the packet with $P_{\mathrm{e}}(z')\,|\mathrm{d}z'| = P_{\mathrm{e}}(t')\,|\mathrm{d}t'|$.

The quantum mechanical derivation is given in the appendix, and the definition of terms is listed in table 1. Here, we present a simple classical picture with a physical interpretation. For a single-energy packet [29], we showed that the PINEM intensity profile can be expressed as

$$P_n(t';\tau) = P_{\mathrm{e}}(t')\cdot Q_n(t';\tau), \tag{4}$$

where $P_{\mathrm{e}}(t')$ is the electron probability density in the time domain (temporal profile or intensity flux) and $Q_n(t';\tau) = |J_n(\Omega(t';\tau))|^2$ is the nth order transition probability of PINEM. J_n is the Bessel function of the first kind with the argument given by $\Omega(t';\tau) = -\frac{e|\tilde{F}|}{\hbar\omega_{\mathrm{p}}}\exp\left[-\frac{(t'+\tau)^2}{4\sigma t_{\mathrm{p}}^2}\right]$. This separation of P_{e} and Q_n has significant consequences. Since Q_n is independent of the electron profile, P_{e}, it can be regarded as the efficiency of a temporal filter, or a pulse slicer; a time domain analogue to an electron energy filter. Here, we only consider the weak interaction limit to derive analytical expressions for the chirp coefficient, pulse slicing and energy refinement. The strong interaction case was treated elsewhere using numerical integration [32]. As shown before [28], in the weak interaction regime, Q_n can be approximated and becomes linearly proportional to $\left|I_{\mathrm{p}}(t')\right|^n$, for $n > 0$. It follows that the PINEM intensity profile becomes:

$$P_n\left(t';\tau\right) \propto P_{\mathrm{e}}\left(t'\right)\cdot\left|I_{\mathrm{p}}\left(t';\tau\right)\right|^n. \tag{5}$$

Given the results for a coherent single-energy packet, we can then consider the incoherent energy distribution associated with a chirp. The electron ensemble (ε) has a mean energy value of $\bar{E}_\varepsilon$. Therefore, we redefine $z' \equiv z - \bar{v}_\varepsilon t$ and $t' \equiv -z'/\bar{v}_\varepsilon$ with respect to the electron ensemble.

Table 1. Definition of terms.

Term	Description
z	Position in a fixed spatial coordinate system
t	Time
$\bar{t}_\mathrm{p}$	Mean arrival time of photon pulse at $z = Z$
σt_p	Temporal width of photon pulse
e	Subscript used for a coherent electron packet
σt_e	Temporal width of electron packet
E	Energy of electron packet
v_E	Energy-dependent velocity of electron packet
$\bar{t}_E$	Energy-dependent mean arrival time of electron packet at given z
$\tau_E \equiv \bar{t}_E - \bar{t}_\mathrm{p}$	Energy-dependent time delay of electron packet at $z = l$
$z'_E \equiv z - v_E t$	Energy-dependent moving frame coordinate system for electron packet
ε	Subscript used for an incoherent ensemble of electron with energy distribution by $P_\varepsilon(E)$
δt_ε	Temporal duration of electron ensemble
δE_ε	Energy spread of electron ensemble
$\bar{E}_\varepsilon$	Mean energy of electron ensemble
$\bar{v}_\varepsilon$	Mean velocity of electron ensemble
$\bar{t}_\varepsilon$	Mean arrival time of electron ensemble at given z
$\bar{\tau}_\varepsilon \equiv \bar{t}_\varepsilon - \bar{t}_\mathrm{p}$	Time delay of electron ensemble at $z = l$
$z' \equiv z - \bar{v}_\varepsilon t$	Position in a moving frame coordinate system for the electron ensemble
$t' \equiv -z'/\bar{v}_\varepsilon$	Relative arrival time for electron ensemble
$E' \equiv E - \bar{E}_\varepsilon$	Energy difference of electron packet with respect to ensemble averaged value
$\Delta v_E \equiv v_E - \bar{v}_\varepsilon$	Velocity difference of electron packet with respect to ensemble averaged value
$\Delta\bar{t}_E \equiv \bar{t}_E - \bar{t}_\varepsilon$	Arrival time difference of electron packet with respect to ensemble averaged value
$\Delta\tau_E \equiv \tau_E - \bar{\tau}_\varepsilon$	Time delay difference of electron packet with respect to ensemble averaged value
$\Delta\bar{E}_\mathrm{g}(\bar{\tau}_\varepsilon)$	Shift of mean energy of gated electrons as a function of the delay

The PINEM intensity of the individual energy component becomes, as derived in appendix A, equation (A.7):

$$P_{E,n}\left(t';\bar{\tau}\right) \approx P_E\left(t';\Delta\bar{t}_E\right)\cdot Q_n\left(t';\bar{\tau}_\varepsilon\right) \tag{6}$$

where $\Delta\bar{t}_E \equiv \bar{t}_E - \bar{t}_\varepsilon$ accounts for the energy-dependent arrival time difference for the electron packet of energy E within the pulse (figures 1(a) and (b)). Equation (6) has the same form as equation (4), except the distribution of $P_E\left(t';\Delta\bar{t}_E\right)$ includes the temporal shift as a parameter, because t' is defined with respect to the ensemble average and the single-energy packet at E is displaced from (not coincident with) it. We note that Q_n only depends on the pump (in this case the hole burning or gating pulse) laser profile and $P_E\left(t';\Delta\bar{t}_E\right)$ depends on the energy distribution of the electron pulse. Consequently, the electrons will exhibit an energy-dependent temporal overlap with the gate optical pulse (figure 1(b)), with an energy selection that depends on the characteristics of the chirp (figures 1(c) and (d)).

Assuming Gaussian profiles for the initial time and energy distributions, we can formulate the phase-space evolution of the chirped electron ensemble, which provides the temporal duration and energy spread following PINEM gating or conventional energy filtering (see appendices B, C and D for detail). For time-slicing, we can express the experimental observable,

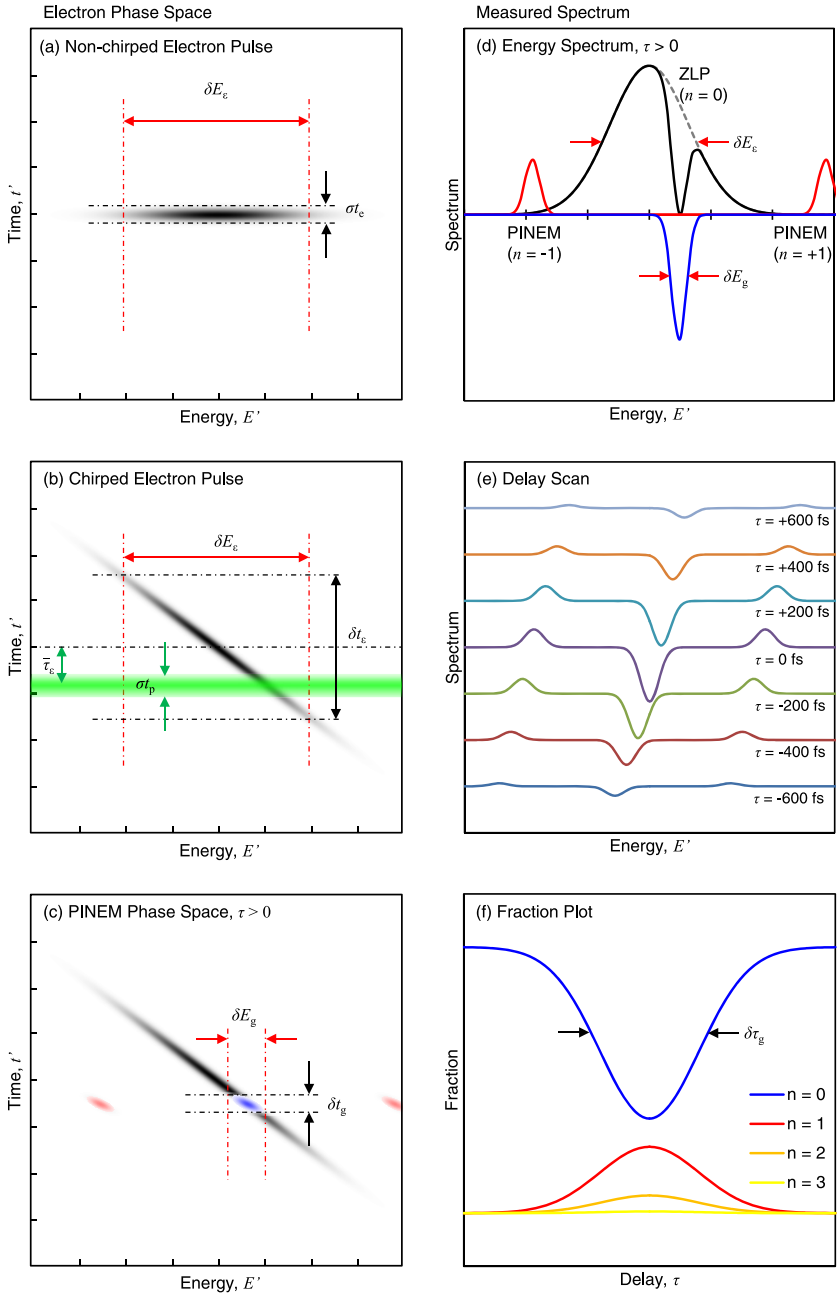

Figure 1. Population density plots of energy-time phase space (equation (B.1)) (a) before and (b) after developing chirp. Energy spread (δE_ε), temporal width (σt_e) and temporal duration (δt_ε) are indicated with dotted lines. Optical duration (σt_p) and electron–photon time delay ($\bar{\tau}_\varepsilon$) are also indicated in green for chirped electrons. (c) Population density plot in energy-time phase space (equation (C.1)) and (d) line plot in the energy domain (integrated along the time domain, equation (C.2)) of the temporally gated electron. ZLP depletion and PINEM peak gain are shown in blue and red, respectively. (e) Electron energy spectra (EES) at different time delays (equation (C.2)). (f) Line plot of the fractions of electrons in the nth state as a function of time delay.

i.e. the energy distribution of PINEM electrons at the given electron–photon nominal temporal delay, $\bar{\tau}_\varepsilon$, as

$$P_{\mathrm{g}}\left(E';\bar{\tau}_\varepsilon\right) \propto G\left[\bar{\tau}_\varepsilon;\delta\tau_{\mathrm{g}}\right]\cdot G\left[E'-\Delta\bar{E}_{\mathrm{g}}\left(\bar{\tau}_\varepsilon\right);\delta E_{\mathrm{g}}\right], \tag{7}$$

where the product is that of two Gaussians for the temporal overlap efficiency and the energy profile of the entire distribution of the pulse, with $\delta\tau_g$ being the duration of the observed PINEM profile, such that $G[\bar{\tau}_\varepsilon;\delta\tau_{\mathrm{g}}]$ results from the convolution of electron and photon temporal profiles (figure 1(f)). We note that $E' \equiv E-\bar{E}_\varepsilon$ is the relative energy (coordinate), $\Delta\bar{E}_{\mathrm{g}}\left(\bar{\tau}_\varepsilon\right)$ is the delay-dependent mean energy shift of gated electrons (figure 1(e)), and δE_g is the time-sliced electron energy spread (figure 1(d)). The apparent slope (mean energy shift per time delay, $\mathrm{d}\bar{E}_{\mathrm{g}}/\mathrm{d}\bar{\tau}_\varepsilon$) is related to the intrinsic chirp coefficient (arrival time shift per energy, $\partial\bar{t}_E/\partial E$) (figure 1(b)) and the temporal duration and energy spread of the chirped electrons; the optical pulse length also affects the apparent slope (see equation (C.2) in appendix C).

4. Results

Figure 2 shows the density plots of the experimentally measured $P_{\mathrm{g}}\left(E;\bar{\tau}_\varepsilon\right)$, the time-sliced energy-distributions of chirped electron ensembles at the given time delay $(\bar{\tau}_\varepsilon)$ between the electron and photon pulses for three different energy spreads of the ZLP (δE_ε); the energy spread was varied using the laser fluence at the photocathode. The density plots of absolute values are given in the left column, whereas those of the differences with respect to a reference frame at negative time delay are shown in the right column. Only when electron and photon pulses were temporally overlapped $(\bar{\tau}_\varepsilon \approx 0)$ was the ZLP depleted (blue in figure 2, right column) and new PINEM peaks populated (red in figure 2, right column) at the energy of $\bar{E}_n = \bar{E}_\varepsilon + nE_{\mathrm{p}}$. Figure 2 clearly displays manifestations of electron chirp; the ZLP depletes, whereas the PINEM grows, and their energy values increase as a function of time delay. The apparent slope of the energy shift increases as the energy spread increases. It also can be seen that the energy spread of PINEM peaks is smaller than the initial electron energy spread (see table 2).

The density plot of difference data was fitted by a least-square method using equation (7) in order to obtain the time-sliced energy spread (δE_{g}), PINEM temporal resolution $(\delta\tau_{\mathrm{g}})$, and the apparent slope $(\mathrm{d}\bar{E}_{\mathrm{g}}/\mathrm{d}\bar{\tau}_\varepsilon)$. The initial energy spread (δE_ε) was determined from the energy profile of ZLP at negative time delays. The fitted slopes are also plotted in figure 2, right column. As described in appendix A, the higher-order PINEM peaks should exhibit a nonlinear dependence on photon pulse length (σt_{p}). However, here, for simplicity, we fitted the data with the same $\delta\tau_{\mathrm{g}}$ for every PINEM peak, since the deviation becomes smaller when the apparent electron duration, δt_ε, is longer than the photon pulse length. From the data we determined the intrinsic temporal width of the electron pulse (δt_ε) and the intrinsic chirp coefficient $(\partial\bar{t}_E/\partial E)$ as a function of δE_ε, using the optical pulse width value corresponding to 280 fs in full width at half maximum (FWHM). The fitted parameters are listed in table 2, and the calculated parameters are compared to those observed in figure S1 in the supplementary material, available at: stacks.iop.org/NJP/14/053046/mmedia.

The intrinsic chirp coefficient, $\partial\bar{t}_E/\partial E$, (slightly) decreases as a function of the energy spread (table 2). The (differential) temporal width, σt_{e}, is substantially longer than the nominal optical duration, and increases (slightly) as a function of energy spread (see figure S2 in the supplementary material). Consequently, the calculated δt_ε (electron duration, see equation (B.3)

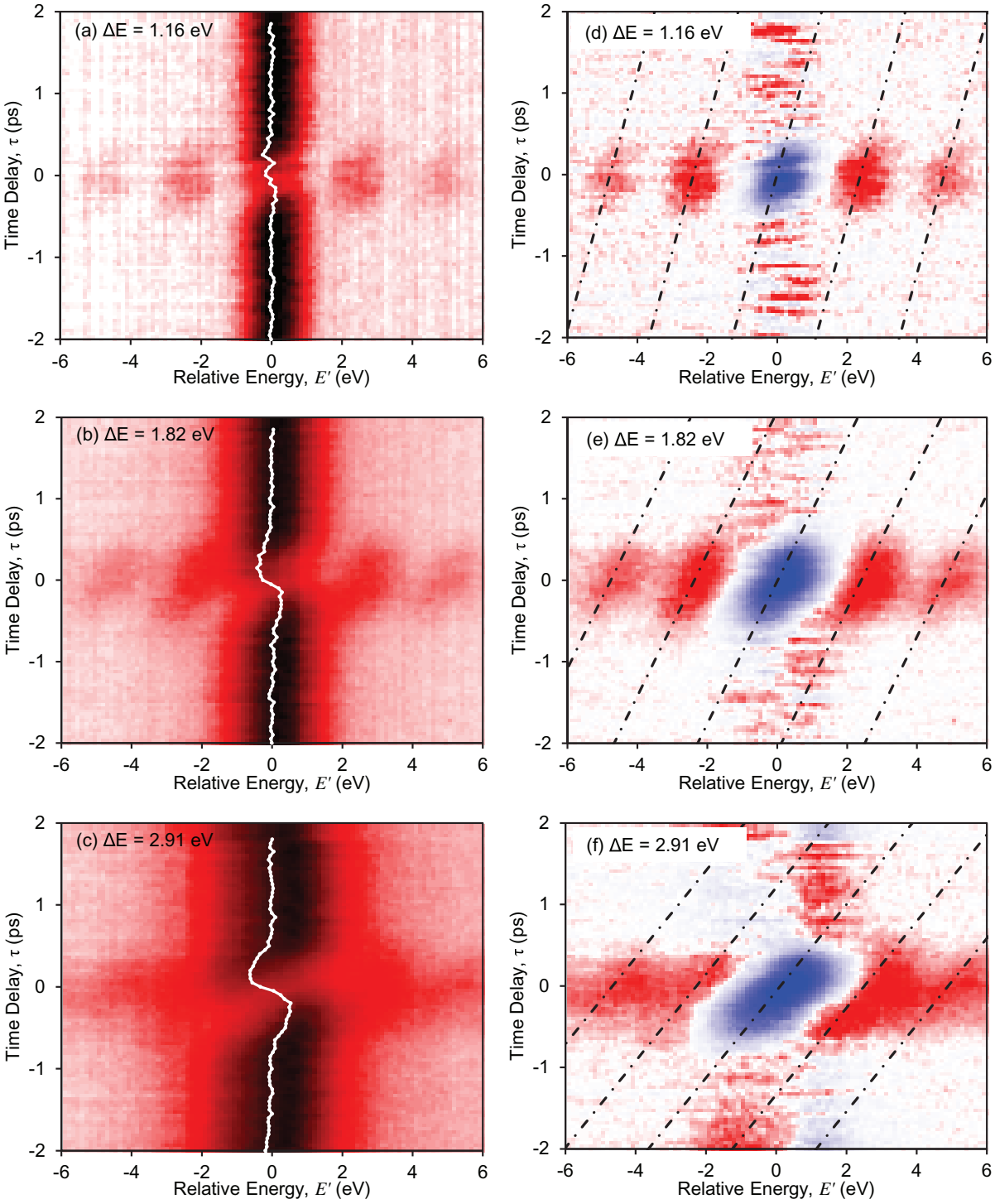

Figure 2. Experimental population density plots of (left) absolute and (right) difference spectra of electron energy as a function of time delay for the electron energy spreads of (top) 1.16 eV, (middle) 1.82 eV and (bottom) 2.91 eV. The mean energy of ZLP is indicated as white solid lines on the left column. The apparent slopes of energy shift as a function of time delay are indicated as a dotted line for ZLP depletion and PINEM growth on the right column.

Table 2. Observed and calculated parameters.[a]

	Observed			Calculated[d]		
U[b] (nJ)	$w\delta E_\varepsilon$[c] (eV)	$w\delta E_g$[c] (eV)	$w\delta\tau_g$ (ps)	$d\bar{E}_g/d\bar{\tau}_\varepsilon$ (eV/ps)	$w\sigma t_e$ (ps)	$\partial\bar{t}_E/\partial E$ (ps/eV)
0.13	1.16 ± 0.02	1.00 ± 0.01	0.58 ± 0.01	0.64 ± 0.03	0.478 ± 0.007	-0.148 ± 0.007
0.25	1.45 ± 0.02	1.21 ± 0.01	0.70 ± 0.01	0.97 ± 0.02	0.556 ± 0.005	-0.209 ± 0.004
0.37	1.82 ± 0.03	1.45 ± 0.01	0.77 ± 0.01	1.15 ± 0.01	0.610 ± 0.004	-0.205 ± 0.003
0.55	2.47 ± 0.04	1.93 ± 0.01	0.70 ± 0.01	1.94 ± 0.02	0.518 ± 0.005	-0.166 ± 0.002
0.67	2.91 ± 0.05	2.06 ± 0.02	0.76 ± 0.01	1.88 ± 0.02	0.585 ± 0.004	-0.153 ± 0.002
0.82	3.49 ± 0.06	2.31 ± 0.02	0.80 ± 0.01	2.02 ± 0.02	0.638 ± 0.004	-0.138 ± 0.002

[a] The width reported here is the full-width-half-maximum (FWHM) of a Gaussian profile, evaluated by multiplying the standard deviation width with a factor of $w = 2\sqrt{2\log 2}$.
[b] Laser pulse energy estimated from the known relation to electron energy spread.
[c] Deconvoluted values taking the detector resolution of $w\sigma E_a = 0.25$ eV in FWHM.
[d] For calculation, $w\sigma t_p = 0.280$ ps (FWHM) is invoked. For other calculated quantities, we employ $\delta t_\varepsilon = \sqrt{\sigma t_e^2 + \left(\frac{\partial\bar{t}_E}{\partial E}\delta E_\varepsilon\right)^2}$ and $\rho^2 = 1 - \left(\frac{\sigma t_e}{\delta t_\varepsilon}\right)^2$, equations (B.3) and (B.4), respectively.

in appendix B) and $\delta\tau_g$ are largely determined by σt_e, rather than by the energy spread term, and the apparent slope, because $\frac{d\bar{E}_g}{d\bar{\tau}_\varepsilon} = \frac{\delta E_\varepsilon^2}{\delta\tau_g^2}(-\frac{\partial\bar{t}_E}{\partial E})$ (see equation (C.1) in appendix C) increases as δE_ε increases. On the contrary, if the electron pulses were highly correlated ($\sigma t_e^2 \ll (\frac{\partial\bar{t}_E}{\partial E})^2\delta E_\varepsilon^2$ and therefore $\delta\tau_g \approx \delta t_\varepsilon \approx (-\frac{\partial\bar{t}_E}{\partial E})\delta E_\varepsilon$), one would observe $\frac{d\bar{E}_g}{d\bar{\tau}_\varepsilon} \approx (-\frac{\partial\bar{t}_E}{\partial E})^{-1}$ (see appendix C). At low laser fluences, the temporal width and the intrinsic slope seem to deviate from those in the space-charge regime. This may be because the two sources of energy spread (excess energy above work function and the space-charge effect) lead to different behaviour in the propagation dynamics (see discussion).

5. Discussion

With the electron pulse fully characterized using the temporal gating method, we can now investigate the coherence of imaging electrons. The origin of the coherence degradation is of particular interest, being either the photon excess energy or the space-charge effect. The analytical expression of the temporal spread due to an energy spread can be derived from the equation of motion [33]. For the space-charge effect, a classical trajectory Monte Carlo simulation can be employed to examine the temporal broadening. However, it is understood that Coulomb repulsion is strongest in the early stages of acceleration and/or propagation, where the electron pulse is small in size, but vanishes as the electron pulse disperses. Therefore, we may approximate that the space-charge effect induces an instantaneous energy spread by which the electron pulse spreads.

It follows that within the impulse model, we can theoretically estimate the intrinsic chirp coefficients. For a simple field-free drift, it becomes

$$\frac{\partial t_l}{\partial E} = -\frac{l}{\bar{\gamma}^3 m_e \bar{v}^3} = -\frac{1}{\bar{\gamma}\,(1+\bar{\gamma})}\frac{\bar{t}_l}{\bar{E}}, \tag{8}$$

where l is the distance, and m_e, v and γ are the electron mass, the velocity and the associated relativistic factor, respectively, such that $\bar{t}_l = l/\bar{v}$, $\bar{p} = \bar{\gamma} m_e \bar{v}$, $\bar{E} = \frac{\bar{p}^2}{(1+\bar{\gamma})m_e}$, $\frac{\partial E}{\partial p} = \bar{v}$, and $\frac{\partial p}{\partial v} = \bar{\gamma}^3 m_e$. Here, E refers to the kinetic energy, not the relativistic energy. For a linear acceleration, we obtain

$$\frac{\partial t_d}{\partial E} = \frac{d}{q_e V}\left(\frac{1}{\bar{v}_f} - \frac{1}{\bar{v}_i}\right) \approx -\left(\frac{d}{\bar{v}_i}\right)\frac{1}{\bar{E}}, \tag{9}$$

where d is the distance of acceleration, q_e is the electron charge, and V is the acceleration voltage, such that $\bar{E} \approx q_e V$. Equation (9) is in a form similar to that of the field-free drift, except that $d/\bar{v}_i$ is a fictitious duration as if electrons were to travel with the initial velocity.[3] Assuming $l = 500\,\text{mm}$ for $\bar{E} = 200\,\text{keV}$, we get $\bar{t}_l = 2.4\,\text{ns}$, and $\bar{\gamma} = 1.39$, and therefore $\frac{\partial t_l}{\partial E} = -0.004\,\text{ps eV}^{-1}$, which is much smaller than was observed in this study ($\frac{\partial \bar{t}_E}{\partial E} \sim -0.2\,\text{ps eV}^{-1}$; see table 2.). Using $V = 1000\,\text{V}$ and $d = 0.5\,\text{mm}$ for the first acceleration stage in UEM-2, and $\bar{v}_i = 5 \times 10^{-4}\,\text{mm ps}^{-1}$ from $\langle E_i \rangle = 0.7\,\text{eV}$ at $E_p - W = 2.1\,\text{eV}$ (see [34]), we can estimate $\frac{\partial t_d}{\partial E} = -1\,\text{ps eV}^{-1}$, which is an overestimation when compared to what is observed. Dispersive propagation with a given energy spread increases the intrinsic chirp coefficient as the electron pulse propagates, whereas (instantaneous) Coulomb repulsion decreases the chirp slope as it broadens the energy with the given temporal spread. The fact that the observed intrinsic chirp coefficient is somewhat smaller than the estimated value may suggest that the space-charge effect is not instantaneous, but rather gradual. Another mechanism may be that a chirp develops during the acceleration due to the initial kinetic energy spread; then its slope is reduced by the space-charge effect during the field-free drift, during which electrons can further repel each other, but hardly spread.

Besides the temporal dispersion, electron pulses may suffer from an inhomogeneous temporal broadening. There are three contributions in temporal broadenings in UEM, which are beam path inhomogeneity, initial kinetic energy spread and the space-charge effect. (a) The electron pulse is generated in a finite size and with a transverse momentum spread. Due to the diffusive lensing effect of the acceleration source in FEG, and the compensating and condensing lenses, electrons at the center of a pulse and those at the perimeter go through different beam paths, thus creating a temporal lag as a function of the radial (transverse) position [35]. (b) The time spent by an electron in acceleration is a nonlinear function of the initial kinetic energy, between 0 to 2 eV, particularly near 0 eV (see figure S3 in the supplementary material, available at: stacks.iop.org/NJP/14/053046/mmedia), and the chirp, therefore, exhibits a nonlinear behaviour. Namely, the initial kinetic energy spread not only increases δt_ε (dispersion), but also deteriorates σt_e (nonlinear chirp). Although time-of-flight is practically a linear function of the initial momentum, neither the final momentum nor the energy is a linear function of the initial momentum. (c) In a simplified model of the space-charge effect, where the repulsive force was assumed to be linearly proportional to the relative position, it would conserve longitudinal emittance, and consequently decrease σt_e, while it increases δE_ε. However, a real electron pulse is not a continuous charge density; it consists of discrete charged

[3] Note that the actual time that an electron spends in accelerating is given by

$$t_d = \frac{d}{q_e V}(p_f - p_i) = \frac{d}{c^2}\frac{2m_e c^2 + E_f + E_i}{p_f + p_i} \to \frac{2d}{v_f + v_i} \approx \frac{2d}{v_f}.$$

particles randomly distributed in space. The discrete randomness induces statistical noise in the space-charge effect, which deteriorates the longitudinal emittance.

To further investigate the electron acceleration/propagation dynamics, we conducted electron trajectory simulations (not shown here), which confirm that the path length inhomogeneity is the dominant factor for increasing σt_e as well as δt_ε, whereas other contributions are relatively small over a few eV of the energy spread range (low current regime). We also found that the space-charge effect increases the energy spread in three steps: after birth (4%), during acceleration (8%) and during drift at crossovers (88%). Temporal dispersion is dominantly determined in the first step, where the velocity is slowest, and the initial chirp coefficient is determined by acceleration dynamics. The final chirp coefficient decreases as a function of charge density, because the space-charge effect increases energy spread during the field-free drift without further dispersion, thus lowering the chirp coefficient. The more energy is spread, the lower the chirp coefficient becomes. Our trajectory simulations indicate that the space-charge effect is fairly linearly proportional to the charge density for energy spread, temporal width, temporal duration and the intrinsic slope of chirped electrons. Therefore, we attribute the observed deviations at low current limits to uncertainties in measurement and/or analysis.

In table 2, it is shown that the energy spread reduction ($\delta E_g/\delta E_\varepsilon$) is not too profound, especially for a small initial energy spread. This is due to the fact that the degree of chirp, or the degree of correlation between energy and time, is rather poor ($\rho = -0.4$ to -0.6 or $R^2 = \rho^2 = 0.1$ to 0.4; see equation (B.4) in appendix B), namely δt_ε is not greater than σt_e, as $\delta E_g = \frac{\sigma \tau_g}{\delta \tau_g}\delta E_\varepsilon = \frac{\sqrt{\sigma t_p^2+\sigma t_e^2}}{\sqrt{\sigma t_p^2+\delta t_\varepsilon^2}}\delta E_\varepsilon$ (see equation (C.1) in appendix C). In order to observe a significant energy spread reduction, one needs to satisfy the condition, $\sigma t_p^2 + \sigma t_e^2 \ll \left(\frac{\partial \bar{t}_E}{\partial E}\delta E_\varepsilon\right)^2$. Since σt_e is substantially deteriorated by beam path inhomogeneity during the acceleration, it is difficult to reduce σt_e to improve the chirp. $\left(\frac{\partial \bar{t}_E}{\partial E}\right)$ is initially determined by acceleration only, and then reduced by the space-charge effect. Furthermore, the space-charge effect also deteriorates σt_e via the statistical noise. Note that UEM-2 adopted the FEG-TEM design with a modification for photoemission; the conventional microscope is designed without considering temporal dispersion due to its continuous nature. In order to improve the degree of chirp, the electron source will have to be optimized to reduce beam path inhomogeneity and space-charge effect. The transverse momentum spread also needs to be minimized by reducing the photon energy above the photocathode work function, e.g., 460 nm excitation for a 2.6 eV work function instead of a 259 nm excitation. However, the photoemission efficiency (current density) is exponentially reduced as excess energy is reduced. Apertures and lenses may be used to filter out transverse momentum spreads, and this will of course reduce the number of electrons.

The analytical expressions for temporal and energy distributions of chirped electron pulses after temporal gating or energy filtering allow us to investigate the effect of the degree of chirp on the temporal and energy resolution. Figures 3(a), (b), (d) and (e) compares energy resolutions by temporal gating for cases of good and poor chirps, where σt_e correspond to 0.05 ps and 1 ps in FWHM, for σt_p of 0.05 ps in FWHM, δE_ε of 2 eV in FWHM and $\frac{\partial \bar{t}_E}{\partial E} = -0.22\,\mathrm{ps\,eV^{-1}}$. When time and energy are well-correlated (figure 3(a), σt_e corresponding to 0.05 ps in FWHM) the energy spread of PINEM electron becomes 0.32 eV, whereas it becomes 1.83 eV for poor correlation (figure 3(b), σt_e corresponding to 1 ps in FWHM). It should be noted, however, that the temporal shortening of PINEM electrons is ~ 0.05 ps for both cases, which is essentially the

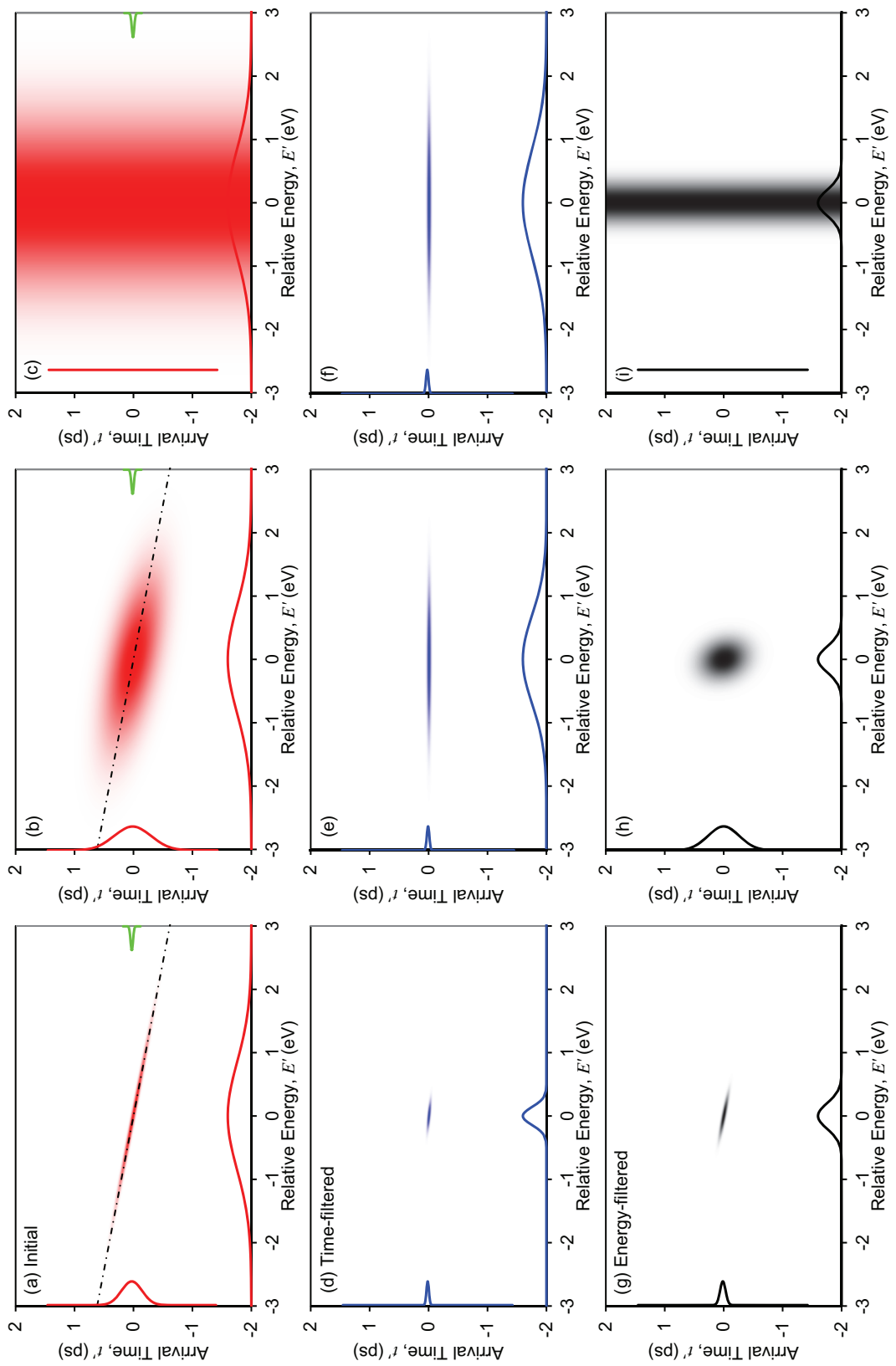

Figure 3. Population density plots of phase space of (top) ZLP, (middle) time-selected, and (bottom) energy-selected electrons with (left) highly correlated chirp, (middle) poorly correlated chirp, and (right) pseudo-continuous beam. Integrated energy and time distributions are plotted on the bottom and the left sides of each panel, respectively.

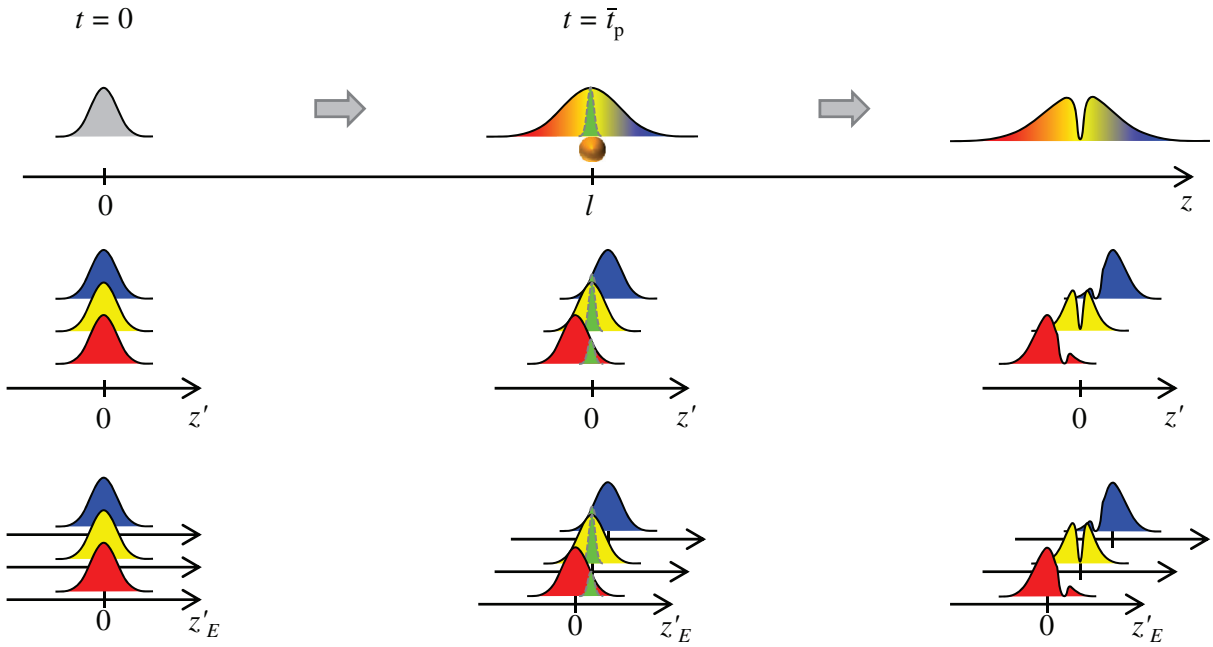

Figure 4. (Top) spatial probability of an electron pulse along the coordinate, z, at three different times, $t = 0$, $\bar{t}_p$, and later. Due to inhomogeneous energy distribution, electron pulse disperses as it propagates. A nanoparticle is at $z = l$, and PINEM transition due to interaction with photon is shown in green. (Middle) spatial probability of three different energy electron packets in the pulse along the ensemble moving coordinate, z', at different times. (Bottom) spatial probability of three different energy electron packets in the pulse along their individual packet moving coordinate, z'_E, at different times.

photon duration, as $\delta t_g = \frac{\sigma t_p}{\delta \tau_g} \delta t_\varepsilon \approx \sigma t_p$ (see equation (C.3) in appendix C). Temporal selection is always possible with PINEM, but energy selection can only be achieved with well-correlated electron beams, as $\delta E_g = \frac{\sigma \tau_g}{\delta \tau_g} \delta E_\varepsilon \approx \frac{\sigma t_e}{\delta t_\varepsilon} \delta E_\varepsilon$ (see equation (C.2) in appendix C), which requires an ultrashort initial electron pulse and little deterioration of the longitudinal emittance.

Figure 3 also compares time-filtering (PINEM, see appendix C) and energy-filtering (conventional, see appendix D) for pulsed and pseudo-continuous electron beams. When the degree of chirp is very high (left column) both time-selection and energy-filtering can generate temporally and energetically highly coherent electron pulses. Temporal selection is only limited by the pulse duration of the laser employed. For energy-filtering, a very fine energy analyzer/selector is required to generate an electron pulse comparable to time-selection. When the degree of chirp is poor (middle column), temporal selection can still produce an ultrashort electron pulse with a modest energy coherence. If there is no chirp relation (right column), such as the case for a pseudo-continuous electron beam, energy-filtering does not improve the pulse length of the electron beam, whereas time slicing can pick the ultrashort electron pulse with the energy spread unchanged.

6. Conclusion and outlook

Here, we demonstrated that the chirp coefficient, as well as the duration of chirped electron pulses, δt_ε, can be directly measured in both time and energy domains using the PINEM effect, which allows us to evaluate the intrinsic temporal width, σt_e. Because PINEM utilizes the electron–photon interaction via a nanostructure at the specimen position, the measured values are made *in situ* and are direct when compared to other methods that employ a deflector, the ponderomotive force or a transient electric field. Since the interaction is through light scattering, the temporal response is instantaneous, allowing a direct measurement of the temporal profiles of the electron and photon pulses.

Similar to the notion that an aperture and an electrostatic sector are a spatial filter and an energy filter, respectively, PINEM acts as a temporal filter for electrons with its efficiency given by $Q_n\,(t', \bar{\tau}_\varepsilon)$ in equation (A.7). Besides the characterization of electron pulses, it is shown that ultrashort and highly coherent electron pulses can be obtained by selecting PINEM electrons, once a chirp is established. The degree of temporal resolution is mainly determined by the pump (gate) laser employed, regardless of the electron pulse characteristics. The degree of energy resolution, on the other hand, depends strongly on the degree of chirp.

In advancing ultrafast electron microscopy, one of the main goals has been to minimize the space-charge effect and the electron dispersion, and ultimately to achieve a time resolution as short as that of the optical pulse duration. The linear space-charge effect pushes leading electrons forward and lagging electrons backward, and thus induces a position-dependent momentum shift, acting as a temporal diffusive lens. With a temporal focusing element, the longitudinal dispersion can be reversed and the ultimate time resolution depends on the final energy spread and the longitudinal emittance. Many schemes of temporal compression of electron pulses depend on the existence and modification of a chirp relation between time and energy. However, this has not been directly measured yet to the best of our knowledge. By measuring the chirp of the electron pulses we can calculate the longitudinal emittance of the electron packet, from which we can estimate the temporal focusability. Furthermore, those quantities can be used to devise/examine/improve the electron pulse compression scheme.

A reflectron can only temporally focus electrons down to σt_e, as it creates energy-dependent time shift in the chirp, and σt_e and δE_ε are conserved. A ponderomotive temporal lens (and a RF compressor), which induces position (time) dependent momentum (energy) shifts, changes δE_ε and consequently σt_e, while conserving the longitudinal emittance. The (temporal) focal length and the (temporal) focus size are inversely proportional to the induced energy spread. However, while the linear space-charge effect without the statistical noise conserves the longitudinal emittance, statistical noise due to discrete randomness in the space-charge effect, as well as inhomogeneity in the beam path, spoils σt_e and consequently the longitudinal emittance; these need to be avoided to achieve the ultimate in ultrafast temporal resolution.

Acknowledgments

This work was supported by the National Science Foundation and the Air Force Office of Scientific Research in the Physical Biology Center for Ultrafast Science and Technology (UST) supported by the Gordon and Betty Moore Foundation at Caltech. The authors would like to thank Drs J Spencer Baskin, Renske M van der Veen, and Ulrich Lorenz for helpful discussion, and Dr Anthony W Fitzpatrick for reading the manuscript carefully.

Appendices

For an electron ensemble (subscript ε), we designate the mean values of energy, velocity, arrival time, and time delay, as $\bar{E}_\varepsilon$, $\bar{v}_\varepsilon$, $\bar{t}_\varepsilon$, and $\bar{\tau}_\varepsilon$, respectively. Throughout this contribution, we employ the following terminology to designate the distributions: 'widths,' σt and σE, refer to partial (differential) widths at single values of other parameters, whereas 'temporal duration' and 'energy spread,' δt and δE, refer to overall widths, integrated over other dimensions. For example, $\sigma t = \sigma t\,(E)$ is the temporal width at a single energy, E, whereas δt is the temporal duration of chirped electrons, integrated over energy spread.

Appendix A. PINEM of a single electron packet

A detailed Schrödinger formulation for a coherent single-energy component is given in [28]. The coherent wavefunction of an electron is given by

$$\psi_E\,(z,t) = g\,(z - v_E t, t)\,\phi_E\,(z,t)\,, \tag{A.1}$$

where v_E is the group velocity of an electron packet at the kinetic energy of E, $g\,(z - v_E t, t)$ is the envelope function in the moving frame of $z'_E \equiv z - v_E t$, $\phi_E\,(z,t) = \exp[\mathrm{i}\,(k_E z - \omega_E t)]$ is the carrier wave, and k_E and ω_E are the nonrelativistic spatial frequency and angular frequency of the electron, respectively, that correspond to the velocity, v_E. A Gaussian envelope function, $g\left(z'_E, t\right) = \sqrt{G\left[z'_E; v_E \sigma t_\mathrm{e}\right]}$, describes a coherent electron packet with a (coherent) temporal width of σt_e (which was previously designated as σ_e), such that the probability is $P_E\,(z,t) = \left|g\left(z'_E, t\right)\right|^2$. Previously, we chose $z = 0$ and $t = 0$ at the electron-photon interaction, defined by the position of the nanoparticle [28]. Here, we choose $z = 0$ and $t = 0$ at the start of propagation, such that $\bar{z}_E\,(t) \equiv \langle z\rangle_E|_t = \int \mathrm{d}z\, z\, P_E\,(z,t) \to v_E t$ exhibits an energy-dependent position at the time of interaction. As in the previous publication, we ignore coherent dispersion of the wavepacket due to energy-time uncertainty, which is negligible on our time scale.

In a slowly-varying light approximation, the electric field of the scattered wave is proportional to the square root of light intensity at the scattering center. The intensity of a gate laser in the interaction region (at $z = l$) can be expressed as

$$I_\mathrm{p}(t) \equiv I_0 \exp\left[-\frac{\left(t - \bar{t}_\mathrm{p}\right)^2}{2\sigma t_\mathrm{p}^2}\right], \tag{A.2}$$

where σt_p is the optical temporal width, and $\bar{t}_\mathrm{p}$ is the arrival time of a photon at the scattering center. From the probability distribution of a propagating wavepacket, the arrival time at z is given by $\bar{t}_E\,(z) \equiv \langle t\rangle_E|_z = \int \mathrm{d}t\, t\, P_E\,(z,t) \to z/v_E$. The time delay for the E component is defined as $\tau_E \equiv \bar{t}_E - \bar{t}_\mathrm{p}$ at $z = l$ and it can be shown that it becomes $\tau_E = \bar{\tau} + (\bar{t}_E - \bar{t}_\varepsilon)$, where we define $\Delta\bar{t}_E \equiv \bar{t}_E - \bar{t}_\varepsilon$, such that $\Delta\tau_E = \Delta\bar{t}_E$.

With $z'_E = z - v_E t$ (see figure 4), equation (A.1) can be written as

$$\psi_E\,(z,t) = g(z'_E, t)\phi_E(z,t). \tag{A.3}$$

By solving the time dependent Schrödinger equation, we obtain the final wavepacket for an individual coherent component by

$$\Psi_E\,(z,t) \to g(z'_E, 0) \sum_{n=-\infty}^{+\infty} \xi_{E,n}(z'_E; \tau_E)\phi_{E_n}(z,t), \tag{A.4}$$

where $E_n = E + nE_\mathrm{p}$ is the electron energy after net photon absorption ($n > 0$) and emission ($n < 0$), $\xi_{E,n}(z'_E;\tau_E) \equiv (\frac{\tilde{F}_E}{|\tilde{F}_E|})^n J_n(\frac{q_\mathrm{e}}{\hbar\omega_\mathrm{p}}|\tilde{F}_E|\exp[-\frac{(z'_E - v_E\tau_E)^2}{4v_E^2\sigma t_\mathrm{p}^2}])$ is the transition amplitude, $\tilde{F}_E(\frac{\omega_p}{v_E}) \equiv \int_{-\infty}^{+\infty} \mathrm{d}z''\tilde{E}_z(z'',\tau_E)\exp[-\mathrm{i}(\frac{\omega_\mathrm{p}}{v_E})z'']$ is the 'PINEM field', and $\tilde{E}_z$ is the longitudinal component of the complex representation of the electric field of the photon scattered by the nanostructure. It follows that $\tilde{F}_E(\frac{\omega_\mathrm{p}}{v_E}) \approx \tilde{F}_\varepsilon(\frac{\omega_\mathrm{p}}{\bar{v}_\varepsilon})\exp[-\mathrm{i}\omega_\mathrm{p}\tau_E]$. The electron probability density in the nth state becomes

$$P_{E,n}(z'_E;\tau_E) = P_E(z'_E)Q_n(z'_E;\tau_E), \tag{A.5}$$

where $P_E(z'_E) = |g(z'_E,t)|^2 = G[z'_E, v_E\sigma t_\mathrm{e}]$ is the initial electron probability and $Q_{E,n}(z'_E;\tau_E) = |\xi_{E,n}(z'_E;\tau_E)|^2$ is the transition probability. Equation (A.5) describes energy-dependent overlap between photons, and an electron packet (with energy of E). However, equation (A.5) is expressed in an energy-dependent moving frame for the individual energy component, and it is more convenient to express it in terms of the moving frame for the whole ensemble.

Since $z = z' + \bar{v}_\varepsilon t = z'_E + v_E t$ (see figure 4) and $\Delta\tau_E = \Delta\bar{t}_E|_{z=l} = -\frac{\Delta\bar{z}_E}{v_E}|_{t=\bar{t}_\varepsilon} = -\frac{\Delta v_E\bar{t}_\varepsilon}{v_E}$, where $\Delta\tau_E \equiv \tau_E - \bar{\tau}_\varepsilon$, $\Delta\bar{z}_E \equiv \bar{z}_E - \bar{z}_\varepsilon$, and $\Delta v_E \equiv v_E - \bar{v}_\varepsilon$, it can be shown that $z'_E - v_E\tau_E = z' - \bar{v}_\varepsilon\bar{\tau}_\varepsilon - \Delta v_E(t - \bar{t}_\mathrm{p}) = z' - \bar{v}_\varepsilon\bar{\tau}_\varepsilon - \Delta v_E(t - \bar{t}_\varepsilon + \bar{\tau}_\varepsilon)$ and therefore $\xi_{E,n}(z'_E;\tau_E) \approx \xi_n(z';\bar{\tau}_\varepsilon + \frac{\Delta v_E}{\bar{v}_\varepsilon}(t - \bar{t}_\mathrm{p}))\exp[-\mathrm{i}\omega_\mathrm{p}\tau_E] \approx \xi_n(z';\bar{\tau}_\varepsilon - (\Delta\bar{t}_E - \Delta\tau_E))\exp[-\mathrm{i}\omega_\mathrm{p}\tau_E]$. (Note that $\Delta\tau_E = \Delta\bar{t}_E|_{z=l}$.) The electron probability density in the nth state when $t \approx \bar{t}_\mathrm{p}$ becomes

$$P_{E,n}(z';\bar{\tau}_\varepsilon) \approx P_E(z';\Delta v_E\bar{t}_\mathrm{p})Q_n(z';\bar{\tau}_\varepsilon), \tag{A.6}$$

where $P_E(z';\Delta v_E\bar{t}_\mathrm{p}) \approx P_E(z';-\bar{v}_\varepsilon\Delta\bar{t}_E) = |g(z' + \bar{v}_\varepsilon\Delta\bar{t}_E, 0)|^2 = G[z' + \bar{v}_\varepsilon\Delta\bar{t}_E, \bar{v}_\varepsilon\sigma t_\mathrm{e}]$ is the shifted initial electron probability and $Q_n(z';\bar{\tau}_\varepsilon) = |\xi_n(z';\bar{\tau}_\varepsilon)|^2$ is the transition probability. Using $t' \equiv -z'/\bar{v}_\varepsilon$, equation (A.6) can be written in terms of a temporal profile as

$$P_{E,n}\left(t';\bar{\tau}_\varepsilon\right) \approx P_E\left(t';\Delta\bar{t}_E\right)Q_n\left(t';\bar{\tau}_\varepsilon\right), \tag{A.7}$$

where

$$P_E(t';\Delta\bar{t}_E) = P_E(z';-\bar{v}_\varepsilon\Delta\bar{t}_E)\left|\frac{\mathrm{d}z'}{\mathrm{d}t'}\right| = G[t' - \Delta\bar{t}_E;\sigma t_\mathrm{e}]$$

is the initial electron probability and $Q_n(t';\bar{\tau}_\varepsilon) = |\xi_n(-\bar{v}_\varepsilon t';\bar{\tau}_\varepsilon)|^2$ is the transition probability. It should be noted that $Q_n(t';\bar{\tau}_\varepsilon)$ is independent of the energy distribution, whereas $P_E(t';\Delta\bar{t}_E)$ shows an energy-dependent shift of center position. For a weak interaction, $\frac{q_\mathrm{e}}{\hbar\omega_\mathrm{p}}|\tilde{F}_z| \ll 1$, the Bessel function becomes $J_n(\Omega) \approx \frac{1}{n!}\left(\frac{\Omega}{2}\right)^n$, such that for the first order, $n = \pm 1$, it becomes

$$Q_{\pm 1} \approx \left|\frac{q_\mathrm{e}}{2\hbar\omega_\mathrm{p}}\left|\tilde{F}_z\right|\exp\left[-\frac{(z' - \bar{v}_\varepsilon\bar{\tau}_\varepsilon)^2}{4\bar{v}_\varepsilon^2\sigma t_\mathrm{p}^2}\right]\right|^2 \propto \left|\tilde{E}_0\exp\left[-\frac{(t' + \bar{\tau}_\varepsilon)^2}{4\sigma t_\mathrm{p}^2}\right]\right|^2 \propto I_\mathrm{p}\left(t';\bar{\tau}_\varepsilon\right). \tag{A.8}$$

Therefore, the transition efficiency becomes linearly proportional to the laser intensity.

The wavefunction of an incoherent ensemble can be described by the density matrix formulation, in which the density matrix operator is given by $\hat{\rho} = \int \mathrm{d}E\,P_0(E)\,|\psi_E(z,t)\rangle\langle\psi_E(z,t)|$. Equivalently, the total wavefunction of an incoherent ensemble is given by

$$\Psi(z,t) = \int \mathrm{d}E\sqrt{P_0(E)}\exp[\mathrm{i}\theta_E]\psi_E(z,t), \tag{A.9}$$

where ψ_E is the coherent electron wavefunction, θ_E is the incoherent random phase for each coherent electron wavefunction, and $P_0(E)$ is the incoherent energy probability distribution, such that $\int \mathrm{d}E\, P_0(E) = 1$. Due to the incoherent nature of the ensemble, the individual coherent wavepackets do not interfere with each other, and the PINEM process occurs independently for each coherent packet, such that the final probability can be written in terms of summation of individual coherent packets. Since the transition efficiency is independent of the incoherent dispersion of the electron packet, one only needs to evaluate the overlap between the transition efficiency and the electron ensemble probability over incoherent energy and time distributions for ensemble average as described below.

Appendix B. Chirp of an electron ensemble

It is convenient to express electron (phase space) probability in terms of arrival time and kinetic energy, instead of position and momentum, such that $t' = -z'/\bar{v}_\varepsilon$ is the electron arrival time deviation from the nominal value at a fixed position, and $E' = \Delta E = E - \bar{E}_\varepsilon \approx \bar{v}_\varepsilon\,(p_E - \bar{p}_\varepsilon) = \bar{v}_\varepsilon \Delta p_E$ is the energy deviation from the mean energy, $\bar{E}_\varepsilon$. We assume that the phase space distribution is given by a Gaussian distribution as

$$P_\varepsilon(t', E') = P_\varepsilon(E')P_E(t' - \Delta\bar{t}_E) = G[E'; \delta E_\varepsilon]G\left[t' - (\frac{\partial \bar{t}_E}{\partial E})E'; \sigma t_\mathrm{e}\right], \tag{B.1}$$

where δE_ε is the electron energy spread, σt_e is the (differential) temporal width, and $\frac{\partial \bar{t}_E}{\partial E}$ is the first order chirp coefficient in time and energy phase space. Namely, the second part of the right hand side describes incoherent temporal dispersion due to incoherent energy spread. A chirp develops via two mechanisms. Firstly, the higher energy component of an electron pulse travels faster and the lower energy component travels slower, temporally separating as a function of energy. Secondly, the space-charge effect pushes the leading electrons forward and the lagging electrons backward, creating a position-dependent energy shift. Figure 1(a) and (b) shows density plots of equation (B.1) before and after a chirp develops. The higher energy component possesses faster velocity, and therefore the arrival time becomes shortened.

The energy profile, $P_\varepsilon(E')$, is simply given by

$$P_\varepsilon(E') = \int \mathrm{d}t' P_\varepsilon(t', E') = G[E'; \delta E_\varepsilon], \tag{B.2}$$

and the temporal profile, $P_\varepsilon(t')$, becomes

$$P_\varepsilon(t') = \int \mathrm{d}E' P_\varepsilon(t', E') = G[t'; \delta t_\varepsilon], \tag{B.3}$$

where $\delta t_\varepsilon = \sqrt{\sigma t_\mathrm{e}^2 + \left(\frac{\partial \bar{t}_E}{\partial E}\delta E_\varepsilon\right)^2}$ corresponds to the duration of the chirped electron ensemble. Using Pearson's product-moment coefficient [36], the degree of correlation can be expressed by

$$\rho = \frac{\mathrm{cov}(E', t')}{\delta E_\varepsilon \delta t_\varepsilon} = \left(\frac{\partial \bar{t}_E}{\partial E}\right)\frac{\delta E_\varepsilon}{\delta t_\varepsilon}, \tag{B.4}$$

such that $\rho^2 = 1 - (\frac{\sigma t_\mathrm{e}}{\delta t_\varepsilon})^2$. $\rho = \pm 1$ indicates that time and energy are perfectly correlated, while $\rho = 0$ indicates that there is no correlation between them, and that they are independent.

Figure 1(b) also shows overlaps between electrons and photons at a positive delay. At the positive time delay ($\bar{t}_p < \bar{t}_\varepsilon$), the electron ensemble arrives later than photons, and therefore the photons overlap only with the higher energy component of the electron pulse, which is faster, and therefore arrives earlier than the center component.

Appendix C. PINEM of an electron ensemble

When the transition probability is assumed to be linearly proportional to the intensity (weak interaction limit), the population change, using equations (A.5) and (A.6), at time delay, τ, becomes

$$P_g(t', E'; \bar{\tau}_\varepsilon) \approx P_\varepsilon(t', E') Q_1(t'; \bar{\tau}_\varepsilon)$$
$$\propto G\left[\bar{\tau}_\varepsilon; \delta\tau_g\right] G\left[E' - \left(\frac{d\bar{E}_g}{d\bar{\tau}_\varepsilon}\right)\bar{\tau}_\varepsilon; \delta E_g\right] G\left[t' - \left(\frac{\partial \bar{t}_g}{\partial \bar{\tau}_\varepsilon}\right)\bar{\tau}_\varepsilon - \left(\frac{\partial \bar{t}_g}{\partial E}\right)E'; \sigma t_g\right], \tag{C.1}$$

where

$$\sigma\tau_g = \sqrt{\sigma t_p^2 + \sigma t_e^2}, \quad \delta\tau_g = \sqrt{\sigma t_p^2 + \delta t_\varepsilon^2}, \quad \delta E_g = \frac{\sigma\tau_g}{\delta\tau_g}\delta E_\varepsilon,$$
$$\frac{d\bar{E}_g}{d\bar{\tau}_\varepsilon} = \left(1 - \left(\frac{\sigma\tau_g}{\delta\tau_g}\right)^2\right)\left(-\frac{\partial \bar{t}_E}{\partial E}\right)^{-1} = \frac{\delta E_\varepsilon^2}{\delta\tau_g^2}\left(-\frac{\partial \bar{t}_E}{\partial E}\right),$$
$$\sigma t_g = \frac{\sigma t_p}{\sigma\tau_g}\sigma t_e, \quad \frac{\partial \bar{t}_g}{\partial \bar{\tau}_\varepsilon} = -\left(\frac{\sigma t_e}{\sigma\tau_g}\right)^2,$$

and

$$\frac{\partial \bar{t}_g}{\partial E} = -\left(\frac{\sigma t_p}{\sigma\tau_g}\right)^2\left(-\frac{\partial \bar{t}_E}{\partial E}\right).$$

Equation (C.1) shows that the electron that interacted with photons exhibits smaller energy spreads and time widths as $\delta E_g \leqslant \delta E_\varepsilon$ and $\sigma t_g \leqslant \sigma t_e$. Figure 1(c) shows the density plot of PINEM energy exchange. Only those electrons that temporally overlap with photons can gain or lose photon energy. The energy profile of population change becomes

$$P_g\left(E'; \bar{\tau}_\varepsilon\right) \propto G\left[\bar{\tau}_\varepsilon; \delta\tau_g\right] G\left[E' - \left(\frac{d\bar{E}_g}{d\bar{\tau}_\varepsilon}\right)\bar{\tau}_\varepsilon; \delta E_g\right], \tag{C.2}$$

and the temporal profile of population change becomes

$$P_g\left(t'; \bar{\tau}_\varepsilon\right) \propto G\left[\bar{\tau}_\varepsilon; \delta t_\varepsilon\right] G\left[t' - \left(\frac{d\bar{t}_g}{d\bar{\tau}_\varepsilon}\right)\bar{\tau}_\varepsilon; \delta t_g\right]. \tag{C.3}$$

where

$$\frac{d\bar{t}_g}{d\bar{\tau}_\varepsilon} = \left(\frac{\delta t_\varepsilon}{\delta\tau_g}\right)^2$$

and $\delta t_g = \left(\frac{\sigma t_p}{\delta\tau_g}\right)\delta t_\varepsilon$. Equation (C.2) shows that the mean energy of a time-selected electron shifts as a function of delay, and that its spread is smaller than that before interaction with photons.

Equation (C.3) shows that a time-selected electron has a pulse duration shorter than both the optical pulse length and the chirped electron duration as $\delta t_g \leqslant \sigma t_p$ and $\delta t_g \leqslant \delta t_\varepsilon$. Equation (C.2) is plotted in figure 1(d) as blue solid lines at positive time delay, where only the narrow energy portion of electron exchanges photon energy and populates $n = \pm 1$ order peaks. It is noteworthy that the energy center of depletion shifts as a function of time delay (figure 1(e)). The $G\left[\bar{\tau}_\varepsilon; \delta t_\varepsilon\right]$ term in equation (C.3) describes the convolution between optical and electron pulses (figure 1(f)).

Appendix D. Energy filtering at the detector

For comparison, we also consider the energy filtering of the incoherent electron packets. When an energy filtering is applied with filter efficiency given by

$$f\left(E'\right) = f_0 \exp\left[-\frac{\left(E' - \bar{F}\right)^2}{2\sigma F^2}\right], \tag{D.1}$$

the filtered population becomes

$$\begin{aligned} P_f\left(t', E'\right) &= P_\varepsilon\left(t', E'\right) f\left(E'\right) \\ &\propto G\left[\bar{F}; \delta F\right] G\left[E' - \left(\frac{\mathrm{d}\bar{E}_f}{\mathrm{d}F}\right)\bar{F}; \delta E_f\right] G\left[t' - \left(\frac{\partial \bar{t}_f}{\partial E}\right)E'; \sigma t_e\right], \end{aligned} \tag{D.2}$$

where $\delta F = \sqrt{\sigma F^2 + \delta E_\varepsilon^2}$, $\delta E_f = \frac{\sigma F}{\delta F}\delta E_\varepsilon$, and $\frac{\mathrm{d}E_f}{\mathrm{d}F} = \left(\frac{\delta E_\varepsilon}{\delta F}\right)^2$. The filtered energy profile becomes

$$P_f\left(E'\right) \propto G\left[\bar{F}; \delta F\right] G\left[E' - \left(\frac{\mathrm{d}\bar{E}_f}{\mathrm{d}\bar{F}}\right)\bar{F}; \delta E_f\right]. \tag{D.3}$$

The filtered temporal profile becomes

$$P_f\left(t'\right) \propto G\left[\bar{F}; \delta F\right] G\left[t' - \left(\frac{\mathrm{d}\bar{t}_f}{\mathrm{d}\bar{F}}\right)\bar{F}; \delta t_f\right], \tag{D.4}$$

where $\delta t_f = \sqrt{\sigma t_e^2 + \left(\frac{\partial \bar{t}_E}{\partial E}\delta E_f\right)^2}$ and $\frac{\mathrm{d}\bar{t}_f}{\mathrm{d}\bar{F}} = \left(\frac{\delta E_\varepsilon}{\delta F}\right)^2\left(\frac{\partial \bar{t}_E}{\partial E}\right)$. Equation (D.4) shows that $\delta t_f \geqslant \sigma t_e$.

References

[1] Zewail A H and Thomas J M 2009 *4D Electron Microscopy: Imaging in Space and Time* (London: Imperial College Press)

[2] Thomas J M and Midgley P A 2011 The modern electron microscope: a cornucopia of chemico-physical insights *Chem. Phys.* **385** 1–10

[3] Carbone F, Kwon O H and Zewail A H 2009 Dynamics of chemical bonding mapped by energy-resolved 4D electron microscopy *Science* **325** 181–4

[4] Kwon O H, Ortalan V and Zewail A H 2011 Macromolecular structural dynamics visualized by pulsed dose control in 4D electron microscopy *Proc. Natl Acad. Sci. USA* **108** 6026–31

[5] Baskin J S, Park H S and Zewail A H 2011 Nanomusical systems visualized and controlled in 4D electron microscopy *Nano Lett.* **11** 2183–91

[6] Zewail A H 2010 Four-dimensional electron microscopy *Science* **328** 187–93

[7] Kassier G H, Haupt K, Erasmus N, Rohwer E G and Schwoerer H 2009 Achromatic reflectron compressor design for bright pulses in femtosecond electron diffraction *J. Appl. Phys.* **105** 113111
[8] Van Cittert P H 1934 The probable vibration distribution in a plane lighted by a direct light source or by means of a lense *Physica* **1** 201–10
[9] Zernike F 1938 The concept of degree of coherence and its application to optical problems *Physica* **5** 785–95
[10] Spence J C H 2003 *High-Resolution Electron Microscopy* (Oxford: Oxford University Press)
[11] Boersch H 1954 Experimentelle bestimmung der energieverteilung in thermisch ausgelösten elektronenstrahlen *Z. Phys. A: Hadrons Nucl.* **139** 115–46
[12] Grogger W, Hofer F, Kothleitner G and Schaffer B 2008 An introduction to high-resolution EELS in transmission electron microscopy *Top. Catal.* **50** 200–7
[13] Schwind G A, Magera G and Swanson L W 2006 Comparison of parameters for Schottky and cold field emission sources *J. Vac. Sci. Technol.* B **24** 2897–901
[14] Kimoto K, Ishizuka K, Asaka T, Nagai T and Matsui Y 2005 0.23 eV energy resolution obtained using a cold field-emission gun and a streak imaging technique *Micron* **36** 465–9
[15] Mitterbauer C, Kothleitner G, Grogger W, Zandbergen H, Freitag B, Tiemeijer P and Hofer F 2003 Electron energy-loss near-edge structures of 3d transition metal oxides recorded at high-energy resolution *Ultramicroscopy* **96** 469–80
[16] Janzen A, Krenzer B, Heinz O, Zhou P, Thien D, Hanisch A, Heringdorf F, von der Linde D and von Hoegen M H 2007 A pulsed electron gun for ultrafast electron diffraction at surfaces *Rev. Sci. Instrum.* **78** 013906
[17] Aidelsburger M, Kirchner F O, Krausz F and Baum P 2010 Single-electron pulses for ultrafast diffraction *Proc. Natl Acad. Sci. USA* **107** 19714–9
[18] Baum P and Zewail A H 2008 Femtosecond diffraction with chirped electron pulses *Chem. Phys. Lett.* **462** 14–7
[19] Weber P M, Carpenter S D and Lucza T 1995 Reflection design for femtosecond electron guns *Proc. SPIE* ed P M Rentzepis *(San Diego CA)* p 23
[20] Wang Y and Gedik N 2012 Electron pulse compression with a practical reflectron design for ultrafast electron diffraction *IEEE J. Sel. Top. Quantum Electron.* **18** 140–7
[21] Wang X J, Xiang D, Kim T K and Ihee H 2006 Potential of femtosecond electron diffraction using near-relativistic electrons from a photocathode RF electron gun *J. Korean Phys. Soc.* **48** 390–6
[22] van Oudheusden T, de Jong E F, van der Geer S B, Op't Root W P E M, Luiten O J and Siwick B J 2007 Electron source concept for single-shot sub-100 fs electron diffraction in the 100 keV range *J. Appl. Phys.* **102** 093501
[23] Baum P and Zewail A H 2007 Attosecond electron pulses for 4D diffraction and microscopy *Proc. Natl. Acad. Sci. USA* **104** 18409–14
[24] Hilbert S A, Uiterwaal C, Barwick B, Batelaan H and Zewail A H 2009 Temporal lenses for attosecond and femtosecond electron pulses *Proc. Natl Acad. Sci. USA* **106** 10558–63
[25] Fill E, Veisz L, Apolonski A and Krausz F 2006 Sub-fs electron pulses for ultrafast electron diffraction *New J. Phys.* **8** 272
[26] Barwick B, Flannigan D J and Zewail A H 2009 Photon-induced near-field electron microscopy *Nature* **462** 902–6
[27] Flannigan D J, Barwick B and Zewail A H 2010 Biological imaging with 4D ultrafast electron microscopy *Proc. Natl Acad. Sci. USA* **107** 9933–7
[28] Park S T, Lin M M and Zewail A H 2010 Photon-induced near-field electron microscopy (PINEM): theoretical and experimental *New J. Phys.* **12** 123028
[29] Park S T and Zewail A H 2011 Enhancing image contrast and slicing electron pulses in 4D near field electron microscopy *Chem. Phys. Lett.* **521** 1–6
[30] Barwick B, Park H S, Kwon O H, Baskin J S and Zewail A H 2008 4D Imaging of transient structures and morphologies in ultrafast electron microscopy *Science* **322** 1227–31
[31] Park H S, Baskin J S, Kwon O H and Zewail A H 2007 Atomic-scale imaging in real and energy space developed in ultrafast electron microscopy *Nano Lett.* **7** 2545–51

[32] Yurtsever A, van der Veen R M and Zewail A H 2012 Subparticle ultrafast spectrum imaging in 4D electron microscopy *Science* **335** 59–64
[33] Gahlmann A, Park S T and Zewail A H 2008 Ultrashort electron pulses for diffraction, crystallography and microscopy: theoretical and experimental resolutions *Phys. Chem. Chem. Phys.* **10** 2894–909
[34] Dowell D H and Schmerge J F 2009 Quantum efficiency and thermal emittance of metal photocathodes *Phys. Rev. ST Accel. Beams* **12** 074201
[35] Weninger C and Baum P 2012 Temporal distortions in magnetic lenses *Ultramicroscopy* **113** 145–51
[36] Pearson K 1920 Notes on the history of correlation *Biometrika* **13** 25–45